frontiers in Materials

REVIEW
published: 31 July 2020
doi: 10.3389/fmats.2020.00247

# Powder Metallurgy: An Alternative for FeMnSiCrNi Shape Memory Alloys Processing

*Bogdan Pricop[1], Ahmet U. Söyler[2,3], Burak Özkal[3] and Leandru G. Bujoreanu[1]**

[1] *Gheorghe Asachi Technical University of Iaşi, Iaşi, Romania,* [2] *TETA Glass Technologies, Istanbul, Turkey,* [3] *Istanbul Technical University, Istanbul, Turkey*

In the case of quintenary Fe-Mn-Si-Cr-Ni shape memory alloys (SMAs), ingot metallurgy (IM) has technological shortcomings concerning compositional segregation, imperfect melt-incorporation of Si, demanganization during heating and cooling-induced cracking, which can be effectively surmounted by combining powder metallurgy (PM) with mechanical alloying (MA). The paper reviews the results reported in the processing and characterization of PM-MA'ed FeMnSiCrNi SMAs, with special emphasis on the findings obtained by present authors in the last decade. Specimens with nominal chemical compositions Fe-18Mn-3Si-7Cr-4Ni and Fe-14Mn-6Si-9Cr-5Ni (mass %) were produced by IM and PM. In the latter case various volume fractions of as-blended powders were MA'ed under protective atmosphere, before being pressed and sintered. Further compacting, up to 5% porosity degrees, was achieved by hot rolling. Structural analysis, performed by X-ray diffraction and scanning electron microscopy, revealed the formation of unusually large amounts of α′-body centred cubic (bcc) thermally induced martensite. This undesirable martensite seemed to be destabilized by tensile pre-straining, and enabled PM specimens to reach higher stresses than IM ones. The formation and accumulation of α′-bcc stress induced martensite was enhanced by tensile pre-straining, mechanical cycling and augmentation of MA'ed powder fraction. It has been argued that the optimization of technological processing parameters of heat treatment (HT) and hot rolling (HR) combined with MA'ed powder fraction caused the augmentation of shape memory effect (SME) magnitude. DMA-temperature scans revealed an increasing tendency of internal friction (tan δ) with MA'ed powder fraction, as well as the presence of two tan δ maxima ascribed to antiferromagnetic-paramagnetic transition and martensite reversion to austenite, respectively. DMA-strain sweeps emphasized the occurrence of a plateau on the storage modulus vs. strain amplitude variation which was associated with stress-induced formation of ε hexagonal close-packed (hcp)-martensite. In spite of large α′-bcc amounts, PM-MA'ed Fe-14Mn-6Si-9Cr-5Ni experienced free-recovery SME which was enhanced by thermomechanical training. Coupling rings, meant to connect vibrating pipes that transport turbulent fluids, being able to mitigate vibrations that could accidentally open the connection, were manufactured and tested.

**Keywords: Fe-Mn-Si alloys, martensite, mechanical alloying, internal friction, coupling ring**

OPEN ACCESS

***Edited by:***
*Chao Yang,*
*South China University of Technology, China*

***Reviewed by:***
*Chenglin Li,*
*Wuhan University, China*
*Laima Luo,*
*Hefei University of Technology, China*

****Correspondence:***
*Leandru G. Bujoreanu*
*lgbujor@tuiasi.ro*

***Specialty section:***
*This article was submitted to Mechanics of Materials, a section of the journal Frontiers in Materials*

***Received:*** *07 May 2020*
***Accepted:*** *07 July 2020*
***Published:*** *31 July 2020*

***Citation:***
*Pricop B, Söyler AU, Özkal B and Bujoreanu LG (2020) Powder Metallurgy: An Alternative for FeMnSiCrNi Shape Memory Alloys Processing. Front. Mater. 7:247. doi: 10.3389/fmats.2020.00247*

## INTRODUCTION

Amongst Intelligent Materials, Shape Memory Alloys (SMAs) form a distinctive group able to restore their original shape by heating or magnetic field application (Ma and Karaman, 2010). Within SMAs class, NiTi-based, CuZn-based, CuAl-based and FeMnSi-based alloys have become of commercial use (Sun et al., 2012). The interest for FeMnSi-based SMAs is due to their lower price, better workability and the perspective to take advantage of the technological development of iron working industry (Dunne, 2012). In FeMnSi-based SMAs, the occurrence of free-recovery shape memory effect (SME) is due to the thermally induced reversion to γ (face centered cubic, fcc) austenite of stress-induced ε (hexagonal close-packed, hcp) martensite (Kajiwara, 1999). Besides ε – hcp, α′ (body centered cubic, bcc) martensite can be generated by cooling, at low Mn amount (Bracke et al., 2006) or by applying high stress levels, where it is stress-induced at the intersection ε plates (Arruda et al., 1999). α′-bcc occurrence is considered as detrimental for the magnitude of SME (Li et al., 2000).

The history of FeMnSi-based SMAs begun in 1982, with the report of SME occurrence in the single crystals of Fe-30Mn-1Si (mass %, as hereinafter, throughout the text) (Sato et al., 1982). The development of polycrystalline alloys was reported 5 years later by Murakami et al. who: (i) discussed the role of Si in reducing the temperature of antiferromagnetic-paramagnetic transition (Murakami et al., 1987c); (ii) obtained a good SME value (above 50%) in the composition range Fe-(28.34) Mn-(4–6.5) Si (Murakami et al., 1987b) and (iii) improved the SME of Fe-32Mn-6Si by means of a combination of pre-strain and heat treatment (Murakami et al., 1987a). In the subsequent 3–4 years, corrosion resistance was improved owing to the benefits of Cr and Ni additions and thus two FeMnSi-based SMA grades were developed in the commercial field: Fe-28Mn-6Si-5Cr (Otsuka et al., 1990) and Fe-l4Mn-6Si-9Cr-5Ni (Moriya et al., 1991).

One of the main drawbacks of FeMnSi-based SMAs was their recoverable strains limited to 5%, even after the application of suitable "training" thermomechanical processing (Stanford et al., 2008) and various attempts, the mentioning of which is beyond the purpose of this paper, were done in order to increase these values. A series of successful results were remarkably obtained through suppressing the formation of the twin boundaries (Wen et al., 2014), associated with austenitic grain coarsening (Peng et al., 2017), which enabled "giant" tensile recoverable strains (Peng et al., 2018) of the order of 7.6–7.7%.

The most prominent practical applications of Fe-Mn-Si-based SMAs include lock rings for bicycle frame pipes (Otsuka, 1991), pipe coupling rings (Druker et al., 2014), fishplates for crane rail fastening (Maruyama et al., 2008), concrete pre-straining rods (Sawaguchi et al., 2006) and embedded stripes for concrete beam curvature control (Shahverdi et al., 2016). More recently, truncated cone modules, produced by high speed – high pressure torsion, were proposed for self-adjustable axial preloading of angular contact bearings (Paleu et al., 2018).

All the above mentioned results were obtained on FeMnSi-based alloy samples produced by ingot metallurgy (IM), comprising melt casting, multiple remelting to achieve the target chemical composition, heat treatment prolonging to homogenize the chemical composition, and slow cooling to avoid contraction cracking (Berns and Theisen, 2008).

As recently pointed out, powder metallurgy (P/M) associated with mechanical alloying (MA), are prone to control both the chemical composition and grain size (Dang et al., 2019), achieving near-final forming parts (Bahador et al., 2020), as well as to minimize secondary processing, thus reducing the amount of generated waste (Aydogmus and Bor, 2011). Nevertheless, as compared to other alloy systems, such as NiTi-based (Bahador et al., 2017) or Cu-based SMA (Mazzer et al., 2017), only few reports exist on the preparation of Fe-Mn-Si-based SMA by P/M-MA processing.

It has been argued that, in spite of the potential embrittlement caused by pores (Xu et al., 2015), applying P/M-MA at FeMnSi-based SMAs enabled an accurate control of chemical composition (Zhang et al., 2003), especially at quintenary Fe-Mn-Si-Cr-Ni SMAs where most of crystal faults were eliminated (He et al., 2006). Moreover, P/M-MA enhanced the solubility of alloying elements into Fe matrix (Liu et al., 1999), reduced the oxide formation tendency (Oro et al., 2014), assisted the occurrence of ε-hcp martensite (Saito et al., 2014) and increased the density of the alloy (Xu et al., 2016).

As opposed to the above mentioned reports, the present authors separately initiated the research-development of P/M-MA'ed FeMnSiCrNi SMAs more than 10 years ago, the first results being communicated at ESOMAT 2009, Prague (Bujoreanu et al., 2009). The present review mainly summarizes the results reported by present authors during the past decade.

## PROCESSING PROCEDURES AND STRUCTURE OF P/M-MA'ed FeMnSiCrNi SMAs

The preparation of prealloyed powders is possible via advanced atomization technics. Compared to the variety of elemental powders, in the market only a few specific composition having commercial importance are available as masteralloy or prealloyed forms offered by powder producers. Same scarceness is true for SMA compositions and therefore many researchers who chose to study P/M route, applied mechanical milling or mechanical alloying (MA) methodology to obtain a powdered material having desired composition in nearly almost each of its particles. Indeed, it is obvious that mechanical alloying is quite logical in order to attain shorter diffusion distances between the constituting elements compared to their elemental powder mixture case.

For fabricating Fe–20Mn–6Si–9Cr alloy powders, it was found that the optimum ball-milling time, at 300 rpm, was 20 h (Dogan and Arslan, 2012). The present authors studied the effect of MA time, up to 8 h for Fe-14Mn-6Si-9Cr-5Ni, using stainless steels milling media in a SPEX-D8000 high energy ball mill at 1,200 rpm. In addition to powder state properties, compatibility and sinterability of these powders were studied and it was concluded that 4 h MA time is optimum since green and sintered densities of the powders started to decreased after this point

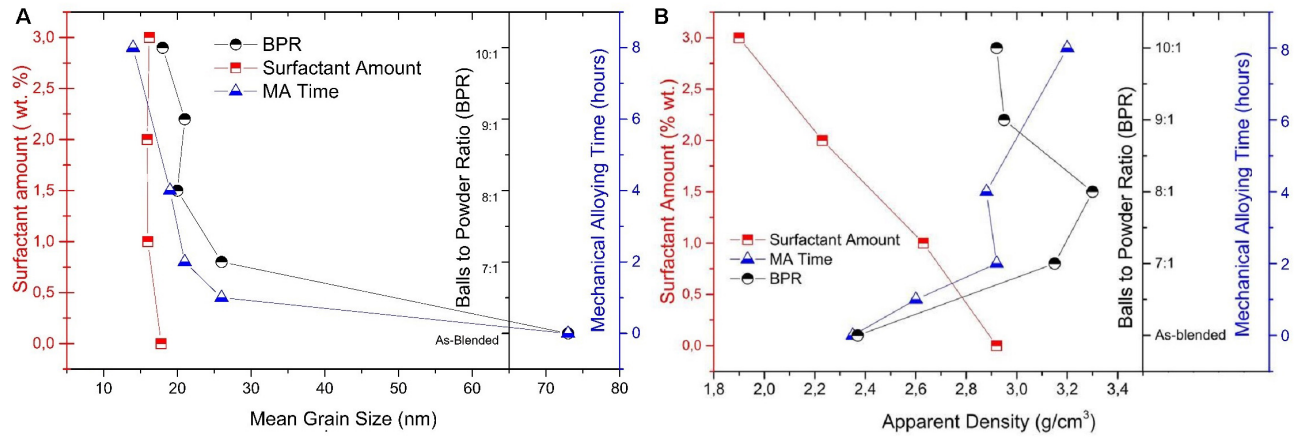


**FIGURE 1 |** Effect of ball to powder ratio (BPR), surfactant amount and mechanical alloying time on **(A)** mean grain size, **(B)** apparent density (modified after Söyler et al., 2010, 2011).

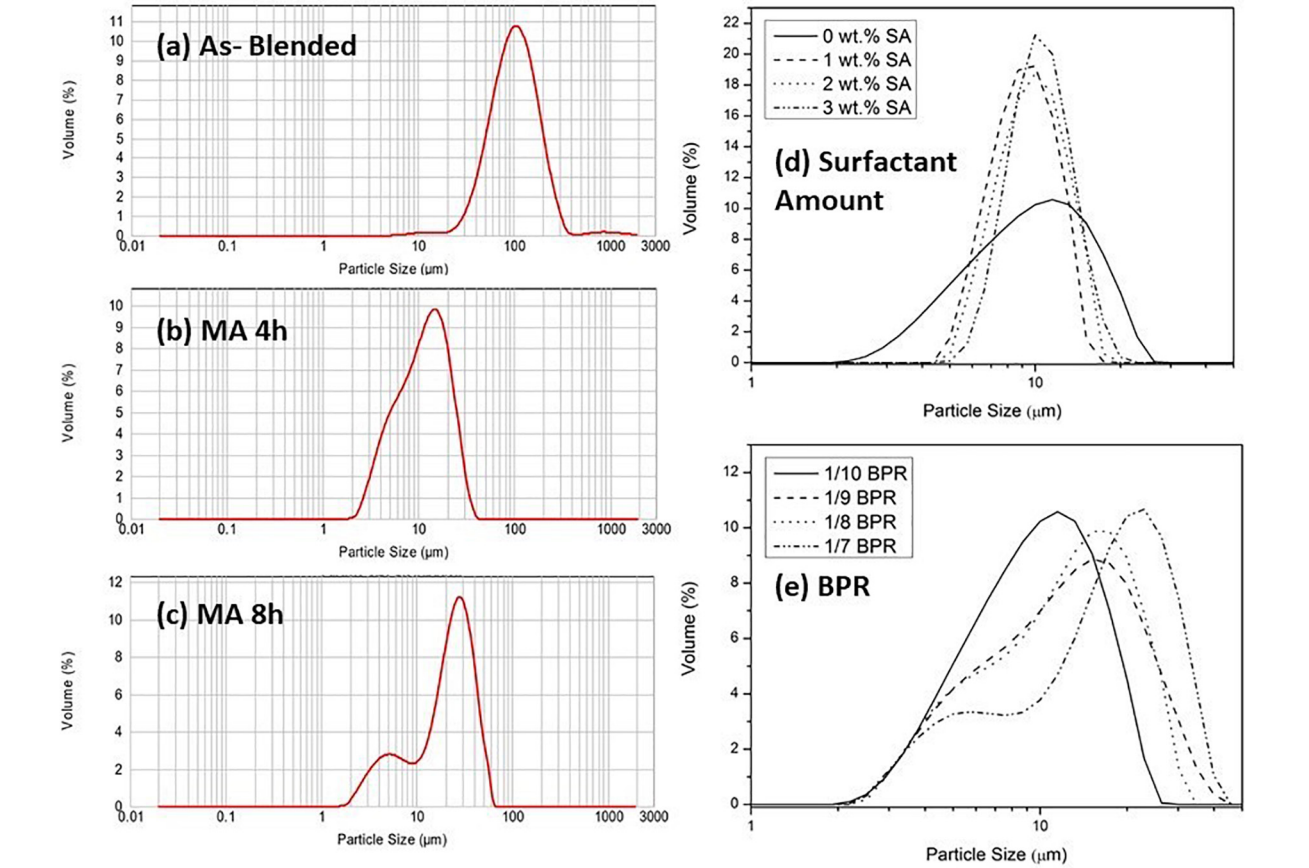


**FIGURE 2 |** Particle size analysis as a function of MA parameters: **(a)** As-blended powders (MA 0 h), **(b)** MA 4 h, **(c)** MA 8 h, **(d)** surfactant amount and **(e)** ball to powder ratio (BPR) (modified after Söyler et al., 2010, 2011).

(Söyler et al., 2010). The effects of ball to powder ratio (BPR), within 10:1 to 7:1 range and amount of surfactant (stearic acid, SA), between 0 and 3% range, were also studied for Fe-14Mn-6Si-9Cr-5Ni, at constant MA time of 4 h (Söyler et al., 2011).

The effect of BPR, surfactant amount and MA time are shown against mean grain size, as calculated from XRD, in **Figure 1A**. Grain size values decreased with increasing BPR and MA time, but a slight increase is observed with the use of surfactant

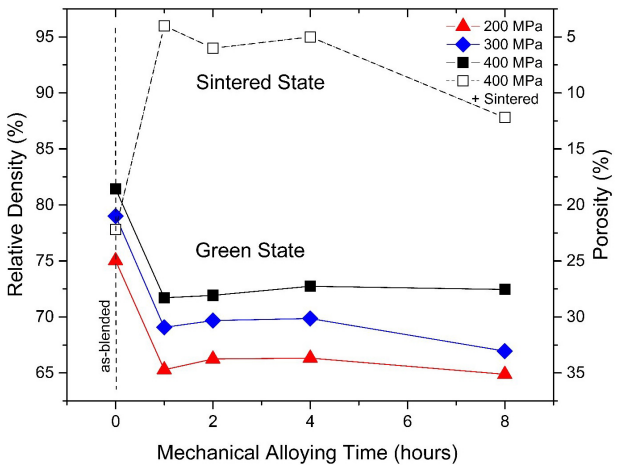


**FIGURE 3 |** Relative density and retained porosity values of the samples after compaction (green state) and after sintering (modified after Söyler et al., 2010).

and with the increase of surfactant amount. The effect of these parameters on apparent density of the powders is shown in **Figure 1B**. While increasing the amount of SA led to a steady decrease for apparent density values, higher BPR and longer MA time led to increase, as compared to the apparent density of as-blended case. Overall effects of these parameters on particle size distributions of the mechanical alloyed powders are also summarized in **Figure 2**. As compared to as-blended case, finer particle sizes are obtained with increasing MA time **Figures 2a–c**. Compared to initial particle size distribution of processed powders without surfactant addition, the use of surfactant and the increase of the surfactant amount led to narrower particle size distributions (**Figure 2d**). Also increasing BPR during MA seems useful for obtaining finer particle sizes without changing the general particle size distribution trends.

For reaching desired level of microstructural homogenization during MA, many parameters should be adjusted in order to maximize the energy input to be delivered to the powders and to minimize the processing time. It is also obvious from the upper discussion that based on energy input provided by milling equipment, the milling conditions should be optimized. On the other hand, utilization of these materials as in powder state is quite rare and subsequent consolidation is necessary to convert them into bulk materials, in order to use them in different engineering applications. Therefore, in addition to the powders state properties, the compaction and sintering behaviors of these powders gain importance. Effect of MA time on compaction and sintering response of these powders were also studied by Söyler et al. (2010). A comparative graph is given in **Figure 3** which shows that the compressibility of the processed powders decreases with increasing MA time. Although better green densities can be obtained with increasing compaction pressure, excessive MA deteriorates the densification during sintering. But in all cases MA has lead to better sintering densification compared to as-blended powders. It should also be noted that full densification at this stage is not necessary or preferably from the perspective of many shape memory alloy compositions, since most of them require post-processing like hot-rolling for training purposes. During post-processing steps further densification can also be compensated and initial sintered microstructure is open for alterations. Therefore, an overall strategy should be applied during MA, considering the final grain size and the relative density of the shape memory material attained at the end.

The importance of grinding time during MA, on the formation of martensite in FeMnSiCrNi SMAs, was also emphasized by other researchers. For instance, Dogan et al. showed that, in the initial stage of ball milling of Fe-20Mn-6Si-9Cr powders, a solid solution of all component elements mainly formed which gradually disappeared with increasing ball milling time. Thus, with the accumulation of lattice strain and process energy, during 20 h-ball milling, particle size decreased to about 100 nm and a large amount of ε (hcp) was generated (Dogan and Arslan, 2012).

However, these phase transformations were observed when subsequent annealing was applied to MA'ed powders at higher temperatures. In the case of P/M-MA'ed FeMnSiCrNi SMAs studied by present authors no newly formed phase was noted, up to 8 h, and most of the diffraction peaks of Mn, Si, Ni, and Cr disappeared in time (Söyler et al., 2010).

On the other hand, a transition from initial α-phase to γ-phase was observed, by Saito et al., during MA of Fe-30Mn-6Si composition. After 20 h MA, the initial α-phase totally transformed γ-phase and this XRD observation was supported with Mössbauer spectra also. Moreover, they mentioned that in the case when no MA was applied, initial Mn peaks can be still observed in the XRD plots even after sintering (Saito et al., 2014).

Both as-blended and MA'ed powders were compacted using uniaxial hydraulic press at 500 MPa in a rectangular prism mold having cross section of 4 mm × 40 mm. Compacted samples were sintered under argon atmosphere at 1,150°C for 2 h using high-temperature furnace and $H_2$ is used at 800°C for 30 min for reduction of the oxides from samples (Söyler et al., 2014).

Sintered P/M-MA'ed specimens with chemical compositions Fe-18Mn-3Si-7Cr-4Ni and Fe-14Mn-6Si-9Cr-5Ni were hot rolled between 1,000 and 1,100°C, with a thickness reduction degree of 20% per pass, until an approximate final thickness of 1 mm. The porosity degree accordingly decreased from 16.85% at 0_MA to 2.51% at 50_MA. The temperature of the last rolling pass was altered, in the case of Fe-14Mn-6Si-9Cr-5Ni at four different values: (i) room temperature (RT), (ii) 600°C, (iii) 800 and 1,100°C (Pricop et al., 2014). After hot rolling, the specimens were heat treated at 700, 800, 900, 1,000 and 1,100°C/5 min/water, in order to relieve internal stresses and to enhance martensite formation. The specimens were further designated with the volume fraction of as blended powder substituted with mechanically alloyed (MA'ed) particles and the heat treatment temperature (e.g., 0_MA_700 describes the specimen sintered from as-blended powders and heat treated at 700°C while 40_MA_1100 designates the specimen with 40%$_{vol}$ MA'ed powder which was heat treated at 1,100°C).

By means of simultaneous thermal analysis (STA), powder mixtures of Fe-14Mn-6Si-9Cr-5Ni, were subjected to three heating-cooling cycles, between RT and 400°C, under two

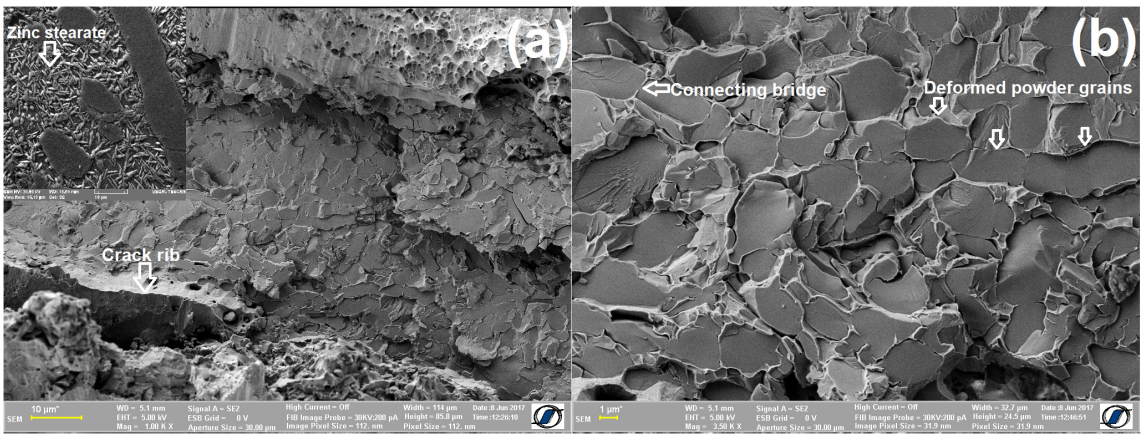


**FIGURE 4 |** SEM micrographs illustrating sintering effects on 0_MA_700 specimen: **(a)** brittle general fractographic aspect with detail of an area with Zn stearate segregation; **(b)** magnified view of an area with connection bridges between deformed powder grains (reproduced after Mocanu et al., 2018, with permission granted by Springer Nature).

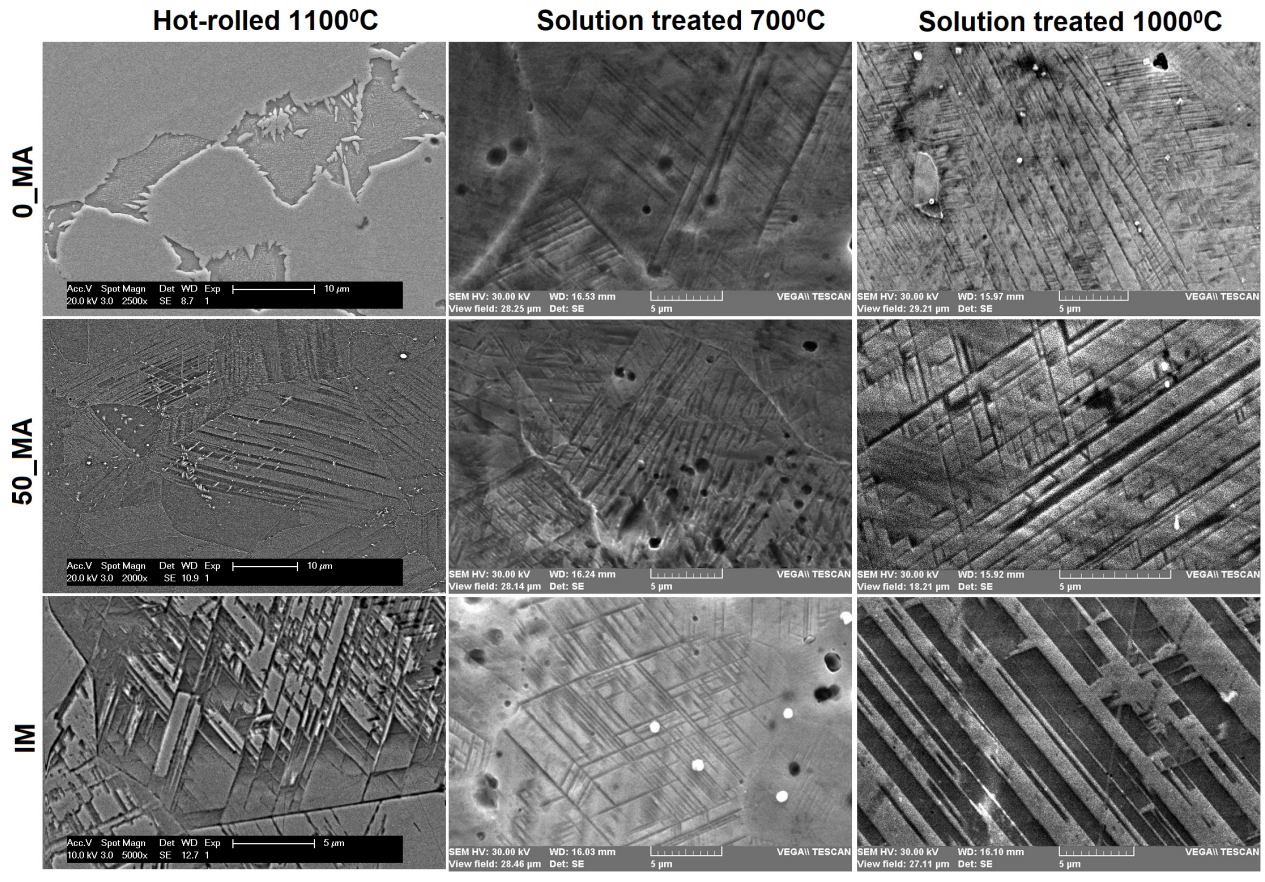


**FIGURE 5 |** SEM micrographs illustrating the evolution of initial hot rolled structure of P/M specimens sintered from pressed as blended powders (0_MA), 50% as blended powders substituted with MA'ed powders (50_MA) and ingot metallurgy specimens (14 Mn), which were subjected to solution treatments at 700 and 1,100°C (adapted after Pricop et al., 2015a, © owned by the authors).

forms: (i) as-blended (0_MA) and (ii) with equal amounts of as-blended and MA'ed powders (50_MA). During each heating and cooling stages, the ferromagnetic-paramagnetic transition of Ni was identified, by means of an exothermic and an endothermic step, respectively. Their thermal ranges experienced an increasing tendency with the number of thermal cycles and

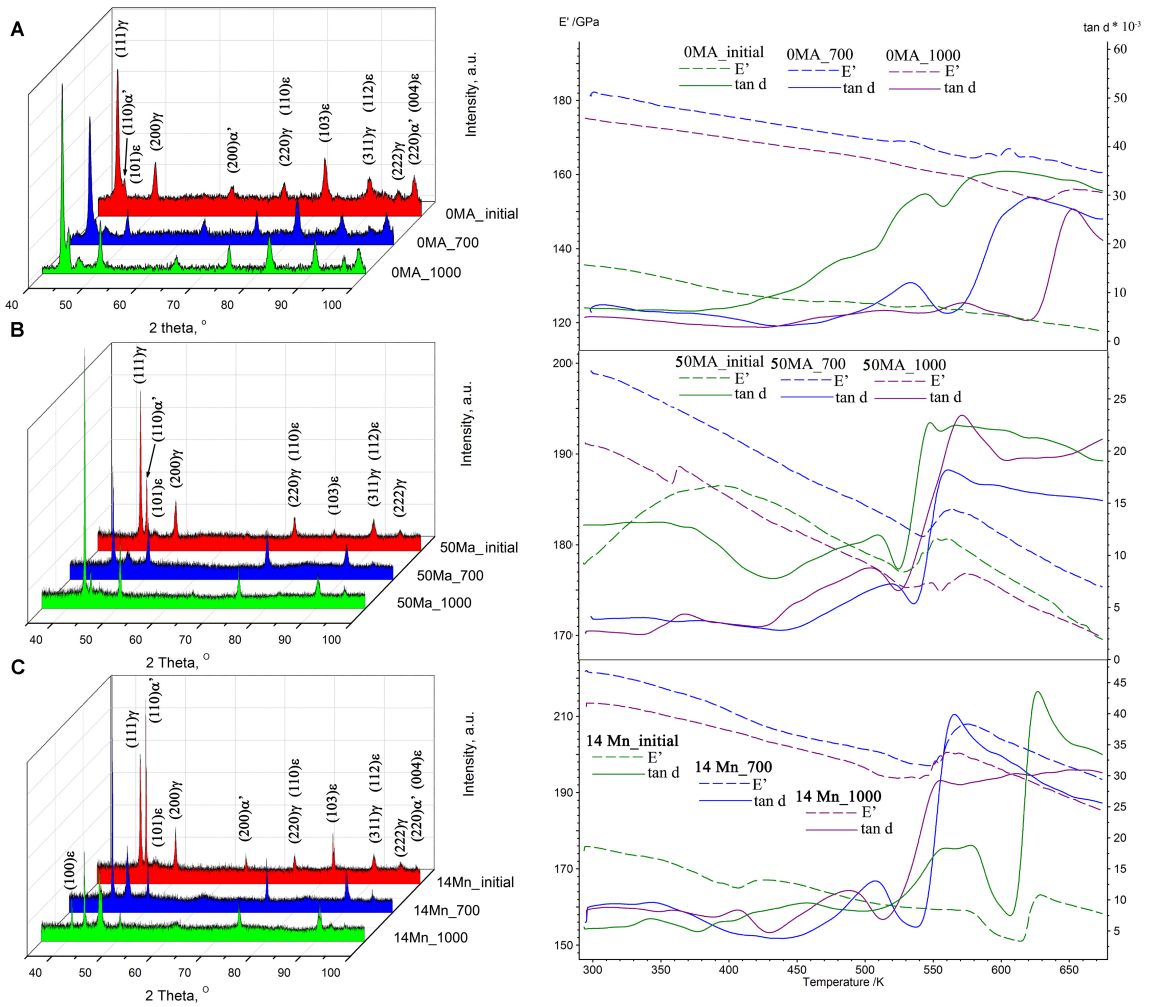


**FIGURE 6 |** Solution treatment effects on the structure and dynamic behavior of: **(A)** P/M specimens sintered from pressed as blended powders (0_MA), **(B)** 50% as blended powders substituted with MA'ed powders (50_MA) and **(C)** ingot metallurgy specimens (14 Mn) (adapted after Pricop et al., 2015a, © owned by the authors).

were higher at 50_MA powders. Besides magnetic transition of Ni, glass transition of amorphous regions was emphasized in MA'ed powders as well as the surface oxidation of as-blended pure Fe particles (Pricop et al., 2011). The powder mixtures were also subjected to heating-cooling cycles in the thermal chamber of a scanning electron microscope equipped with focused ion beam (SEM-FIB), the effects being evaluated by SEM and X-ray diffraction (XRD). The former emphasized the presence of iron oxides under the form of micrometer-size length cilia-like outgrowth and the latter highlighted the partial crystallization of amorphous regions in 50_MA powder mixtures (Pricop et al., 2012).

After pressing and sintering, the powders were aggregated into single compacts the density of which was further increased by hot rolling. It was noticed that the specimens obtained from sintered as-blended powders remained highly brittle, even after hot rolling and heat treatment. The brittle character of the specimens could be revealed by fractographic observations such as the example illustrated, in **Figure 4**, in the case of a 0_MA_700 specimen.

**Figure 4a** shows long crack ribs and an area with Zn stearate segregation. **Figure 4b** displays the presence of connection bridges between elongated powder grains, as an effect of rolling (Mocanu et al., 2018).

The main shortcoming seems to be the high brittleness of sintered powder compacts due to a porosity degree of 16.85%. Future efforts will be focused on the optimization of MA processing parameters, considering the initial particle size of the powders and energy provided by high energy milling equipment.

## THERMOMECHANICAL PROCESSING AND PRE-STRAINING EFFECTS

Most of our work consisted in comparing the effects of hot rolling and heat treatments upon structure and properties of IM and P/M specimens, while substituting various amounts of as-blended with MA'ed powder fractions, in the latter case.

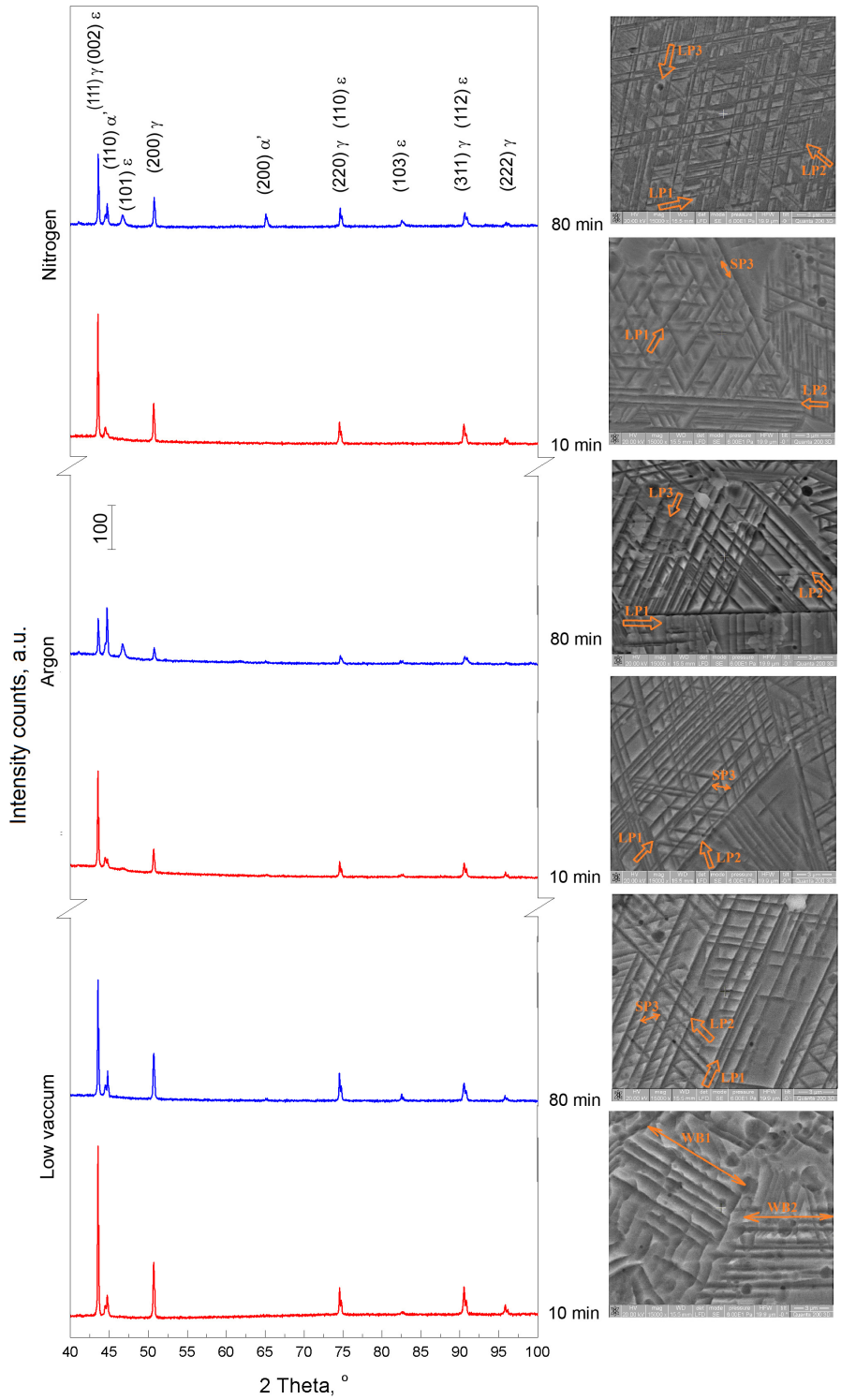


**FIGURE 7 |** Effects of holding environment (protective atmosphere: low vacuum, argon and nitrogen) and time (10, 80 min) on the structure of 50_MA specimens heat treated at 1,200°C (reproduced after Pricop et al., 2016, with permission granted by Springer Nature).

The first investigations were performed on IM and P/M-MA'ed specimens Fe-18Mn-3Si-7Cr-4Ni SMA. Firstly, when subjected to tensile cycling, it was noticed that both IM and P/M specimens experienced transformation induced plasticity, within the first tensile loading cycle and slip induced plasticity during the subsequent ones. Yet IM specimens preserved their

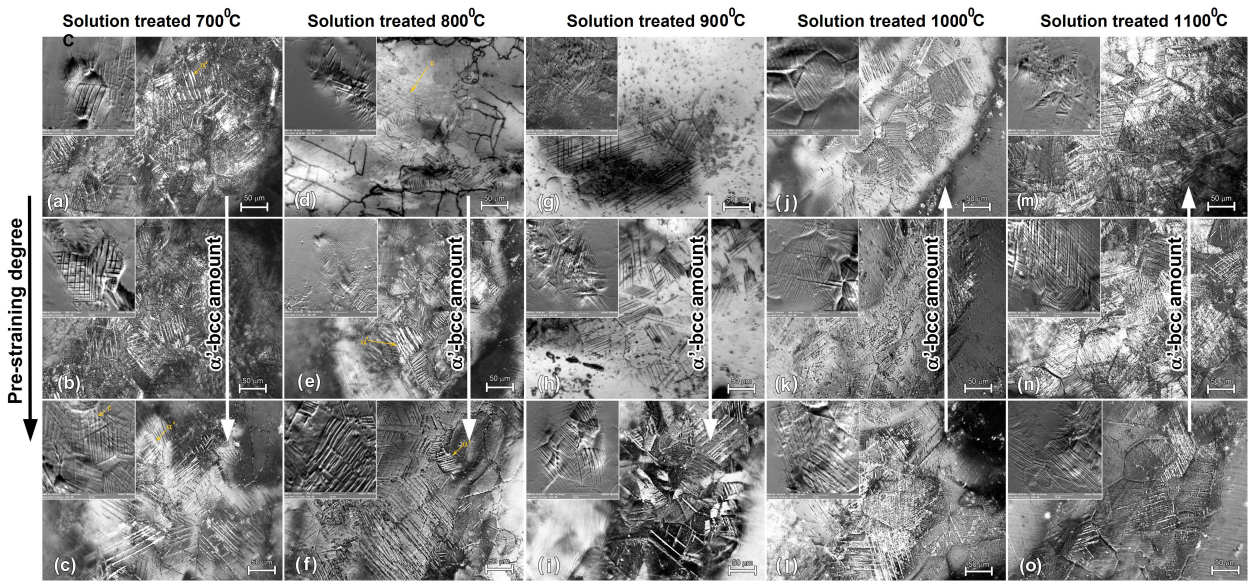


**FIGURE 8 |** Dark-field OM micrographs with SEM insets illustrating the formation of thermally induced martensite with increasing solution treatment temperature (from 700 to 1,100°C) and the occurrence of stress induced martensite with increasing pre-strain degree (from 0% to max. 4.2%) at specimens sintered from as-blended powders, 0_MA_700 at **(a)** 0%; **(b)** 0.7%; **(c)** 2%; 0_MA_800 at: **(d)** 0%; **(e)** 2.1%; **(f)** 3.3%; 0_MA_900 at: **(g)** 0%; **(h)** 1.8%; **(i)** 3.4%; 0_MA_1000 at: **(j)** 0%; **(k)** 1.7%; **(l)** 4.2%; 0_MA_1100 at: **(m)** 0%; **(n)** 1.1%; **(o)** 3.8% (reproduced after Pricop et al., 2015b, Open Acess).

pseudoelastic character even after total strains of 25% while P/M ones were tougher, due to the presence of larger amounts of α′-bcc stress induced martensite. The elongated gauges of tensile specimens were further analyzed by dilatometry (DIL) and XRD. The former revealed a solid state transition occurring during first heating, that increased in intensity with the maximum applied strain, while the latter confirmed the presence of larger amounts, i.e., 10–13%, of α′-bcc stress induced martensite in P/M-MA'ed specimens (Bujoreanu et al., 2009). Aiming to further investigate the stress induced formation of α′-bcc martensite and its thermally induced reversion to γ-fcc austenite, a study was performed on P/M Fe-18Mn-3Si-7Cr-4Ni specimens sintered from as-blended powders with Zn stearate binder (P/M -Zn) and from MA'ed powders without binder (P/M-MA). At P/M -Zn specimens, XRD patterns revealed that the amount of α′-bcc stress induced martensite increased with the number of tensile cycles, exceeding 34% after 20 cycles. On the other hand, at P/M-MA specimens, XRD emphasized a decreasing tendency of α′-bcc martensite with increasing the number of tensile mechanical cycling. It was demonstrated that none of P/M-MA Fe-18Mn-3Si-7Cr-4Ni specimens revealed ε-hcp martensite on their XRD patterns. Nevertheless, a slight contraction was observed by DIL, at about 360°C, during heating of the gauge of the tensile specimen subjected to five mechanical cycles. It has been assumed that this low-intensity SME (since an elongated specimen tends to reduce its length during heating) could be caused by the thermally induced reversion of α′-bcc stress induced martensite (Pricop et al., 2010).

The greatest part of experiments were performed on specimens with chemical composition Fe-14Mn-6Si-9Cr-5Ni. Three specimens in each state, 0_MA, 50_MA and IM, respectively, were hot rolled and then one specimen was heat treated at 700°C and the other at 1,000°C. The nine resulting representative microstructures, recorded by SEM, are summarized in **Figure 5** (Pricop et al., 2015a).

In hot rolled state, martensite plates are noticeable only at specimens 50_MA and IM, which has an average grain size of 74.4 μm, much larger than 17.8 μm, the corresponding value for P/M specimens. After solution treatment at 700°C, the density of martensite plates obviously increased. At IM specimen, average grain size decreased to 29.4 μm, due to recrystallization and this caused a refinement of martensite plates. Increasing heat treatment temperature to 1,000°C produced finer preferentially oriented martensite plates, in 0_MA and 50_MA specimens but caused the increase of martensite plates widths at IM specimen, since a slight grain coalescence occurred, causing average grain size increase to 40.3 μm. The identification of phase structure was performed by XRD and the dynamic behavior of the nine specimens under study was evaluated by dynamic mechanical analysis (DMA), using three-point-bending specimen holder, as summarized in **Figure 6** (Pricop et al., 2015a).

In **Figure 6A**, on the XRD pattern of 0_MA specimen in hot rolled state, designated as "initial," the relative intensities of the diffraction maxima corresponding to ε-hcp and α′-bcc martensite plate variants are rather low. After heat treatment, the intensities of $(101)_{\varepsilon}$ and $(110)_{\alpha'}$ planes that correspond to the main maxima of the two martensites, increased and the effect is more obvious at 0_MA_1000. These XRD patterns of 0_MA specimens confirm the absence of martensite plates at hot rolled specimen and their presence in heat treated states. The DMA thermograms from **Figure 6A** illustrate a continuous decrease of storage modulus ($E'$) during heating at all specimens,

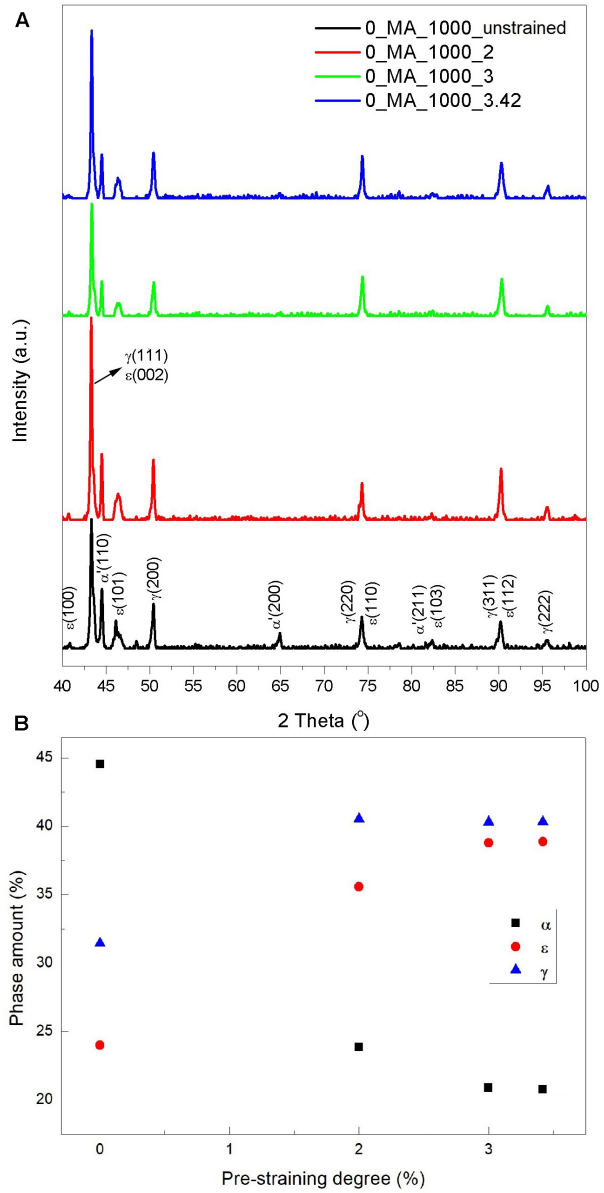


**FIGURE 9 |** Effects of pre-straining degree increase at 0_MA_1000 specimens: **(A)** XRD patterns and **(B)** phase amounts of α′-bcc martensite, ε-hcp martensite and γ-fcc austenite (reproduced after Pricop et al., 2018, with permission granted by Taylor & Francis).

since martensite is stiffer than austenite and two internal friction (tanδ) maxima, associated with the successive reversions to γ (fcc) austenite of α′-bcc and ε-hcp martensites, respectively (Pricop et al., 2015a). More recent studies corroborated the variations of storage modulus and magnetization, during heating. By associating storage modulus and magnetization increases, observed during heating (Mocanu et al., 2018), it was suggested that the occurrence of the first tanδ maximum could be a composed effect of overlapping α′-(bcc) →γ (fcc) reverse martensitic transformation and antiferromagnetic → paramagnetic transition at Néel temperature ($T_N$) (Pricop et al., 2018). At 50_MA specimens, the main diffraction maxima of martensite are more prominent than in the case of 0_MA, in good agreement with the micrographs from **Figure 5**. In addition, some maxima are broader, in **Figure 6B**, which could indicate either small crystallite size along the direction normal to the specified planes or distortions of crystalline structure, as an effect of MA. Due to the higher amount of martensite, the internal friction maxima are obviously more prominent in **Figure 6B** than in **Figure 6A** and storage modulus experiences an obvious increase, ($\Delta E'_{max}$ = 19 GPa). When comparing the three XRD patterns from **Figure 6C**, recorded at IM specimens designated as 14 Mn, it is noticeable that the hot rolled state presents a large $(110)_{\alpha'}$ diffraction maximum, that sustains the presence of α′-(bcc) martensite in this specimen, while no diffraction maxima belonging to α′-(bcc) martensite could be identified, in heat treated specimens. However, the storage modulus of hot rolled (initial) 14 Mn specimen experienced an increase of $\Delta E'$ = 12 GPa, in spite of its general low values. It was noticed that heat treatment caused an increase of maximum storage modulus values, and a decrease of maximum internal friction, from 0_MA, to 50_MA and finally to 14 Mn (Pricop et al., 2015a).

It was also noticed that martensite plate variants became more diversified with the increase of MA fraction and more complexly intersected, as more γ-fcc austenite transformed to α′-bcc and ε-hcp stress-induced martensites (Bulbuc et al., 2019).

In the particular case of 50_MA specimens, the effects of holding environment (protective atmosphere) and time, during the heat treatment at 1,200°C followed by water quenching, were investigated, as summarized in **Figure 7** (Pricop et al., 2016).

The XRD patterns reveal that the heat treatments performed during 80 min, in nitrogen or argon atmospheres, caused the occurrence of ε-hcp martensite, while α′-(bcc) martensite is present in all specimens, ranging between 17 and 65%. The semi-quantitative analysis was performed based on the ratio of the intensities of the non-overlapping peaks $(110)_{\alpha'}$, $(101)_{\varepsilon}$, $(200)_{\gamma}$, $(200)_{\alpha'}$, $(103)_{\varepsilon}$ and $(222)_{\gamma}$ (Sawaguchi et al., 2008). The amount of ε-hcp martensite represents 8–20%, after the heat treatment performed during 80 min, and this could sustain the presence of SME, in these specimens. Even if the ε-hcp martensite could not be detected on XRD patterns, the SEM micrographs display "triangular" morphologies" formed by martensite plates oriented over three directions $\{111\}_{\gamma}$, marked with indexes 1, 2, and 3. The specimen heat treated for 10 min in low vacuum presents wide martensite plates (WB1 and WB2) while those treated in argon and nitrogen display thinner bands. Typical structures comprise long plates of two variants (LP1 and LP2) and a shorter plate (SP3) separated by the long ones. These results sustain the conclusion that MA promotes the formation of α′-(bcc) martensite, after heat treatment at 1,200°C in low vacuum, argon or nitrogen, both at short and long holding periods, while ε-hcp martensite formed only after 80 min holding in argon or nitrogen (Pricop et al., 2016).

On the other hand, the highest structural homogeneity degree was achieved after 80 min holding in low vacuum (Spiridon et al., 2013).

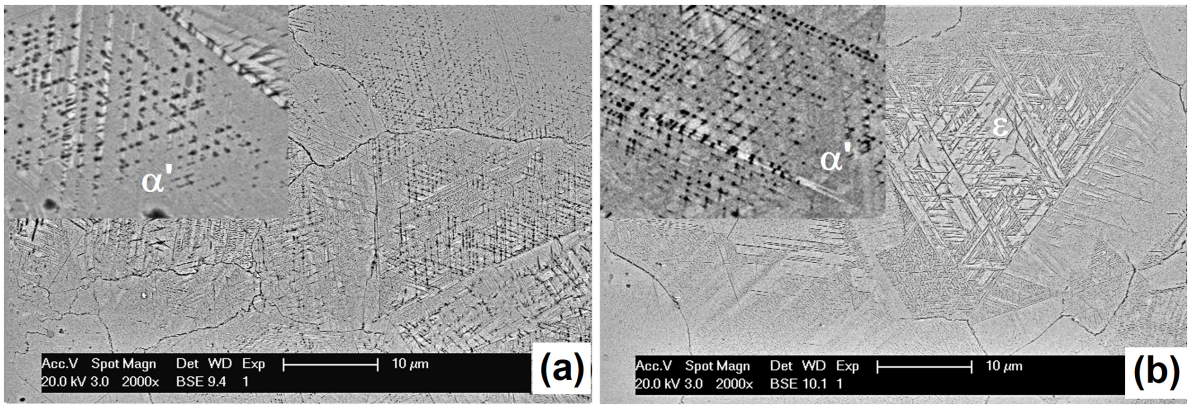


**FIGURE 10 |** Influence of MA degree on the microstructure of specimens pre-strained with 4%: **(a)** 0_MA_1100 and **(b)** 50_MA_1100, with thermally induced ε-hcp martensite. The insets display the effects of 4% pre-straining on stress-induced formation of α′-bcc martensite (modified after Pricop et al., 2013).

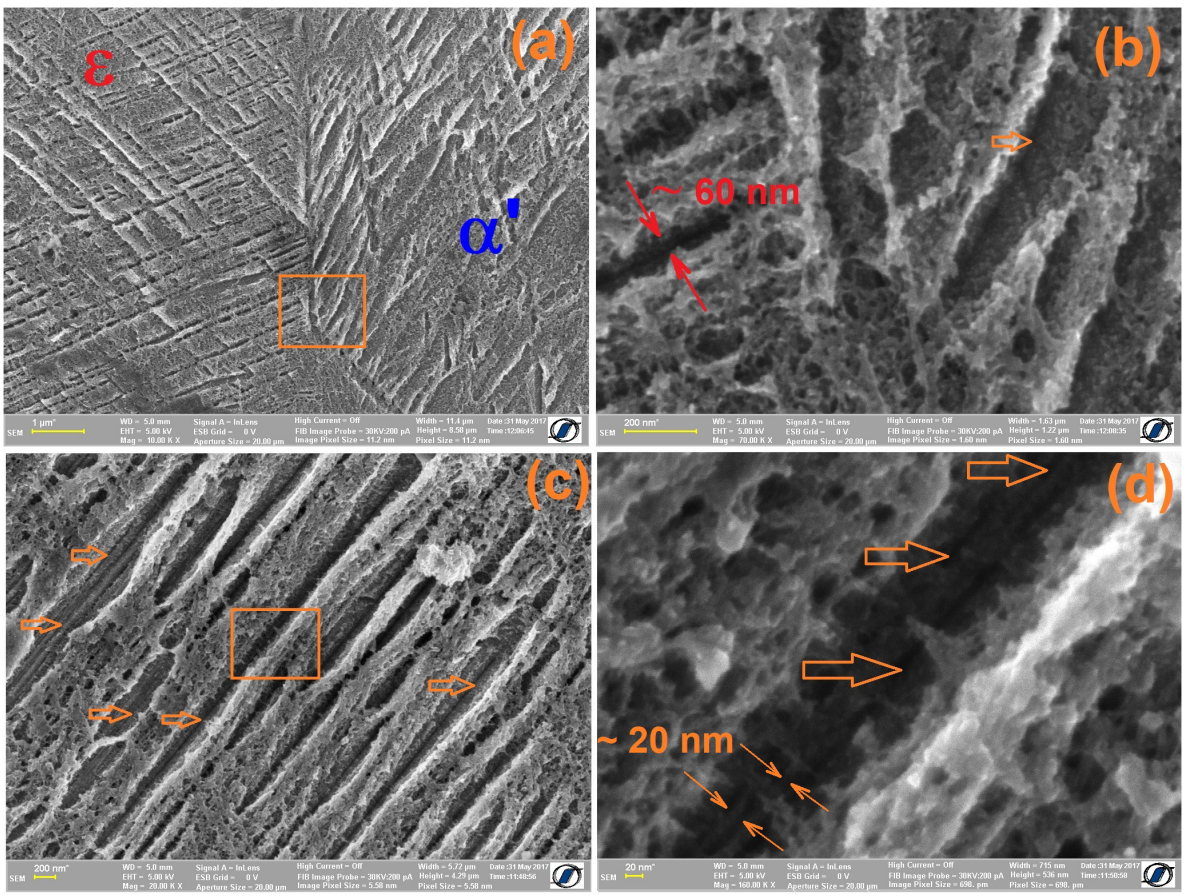


**FIGURE 11 |** (Sub)structural particularities of specimen 0_MA_1100 illustrated by HR-SEM: **(a)** grain boundary between neighboring regions with α′-bcc and ε-hcp thermally induced martensite; **(b)** detail of the grain boundary from panel **(a)** with typical dimension of a ε-hcp martensite plate and one internal sub-band of α′-bcc martensite; **(c)** multiple sub-bands identified within α′-bcc martensite plates with single orientation and **(d)** detail from panel **(c)** typical dimension of identified α′-bcc martensite sub-bands from panel **(c)** (reproduced after Pricop et al., 2018, with permission granted by Taylor & Francis).

The cumulated effects of heat treatments and tensile pre-straining degrees were investigated on the hot rolled specimens sintered from as-blended powders, designated as 0_MA_700, 0_MA_800, 0_MA_900, 0_MA_1000 and 0_MA_1100. The XRD patterns showed that, with increasing heat treatment temperature, the amount of α′-bcc martensite experienced

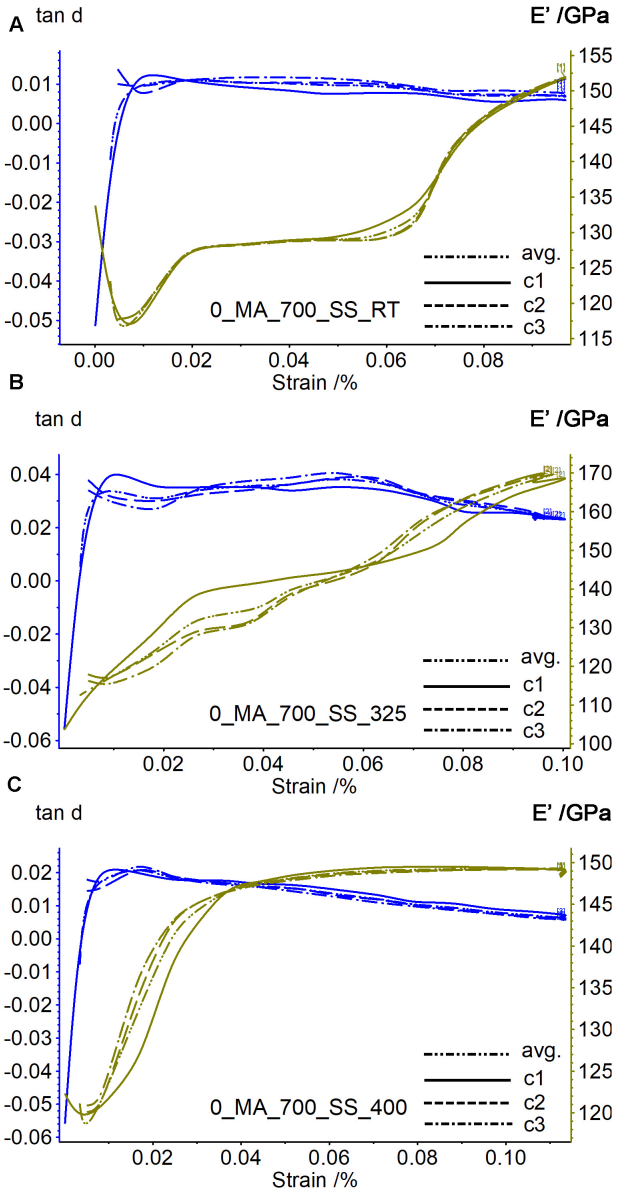


**FIGURE 12 |** Influence of test temperature on the dynamic behavior of 0_MA_700 specimens, during DMA SS, at: **(A)** $T_1$ = RT; **(B)** $T_2$ = 325°C and **(C)** $T_3$ = 400°C (reproduced after Pricop et al., 2018, with permission granted by Taylor & Francis).

an increasing tendency reaching a maximum at 1,100°C. The further application of tensile pre-straining revealed two opposing tendencies: (i) at specimens 0_MA_700, 0_MA_800 and 0_MA_900 the amount of α′-bcc martensite increased with pre-straining degree and (ii) at specimens 0_MA_1000 and 0_MA_1100 it decreased. This situation is summarized in **Figure 8** (Pricop et al., 2015b).

As mentioned above, ε-hcp martensite is visible due to its typical "triangular" morphology caused by the $\{111\}_\gamma$ habit planes and its narrow plates that completely cross austenite grains, from one border to the other. α′-bcc martensite, with shorter bands with either lenticular or lath shape, does not cross austenite grains and is better emphasized in dark field. By means of EDS measurements, it has been proved that the bcc phase identified on XRD patterns is martensite and not a ferrite, because no chemical composition fluctuations were detected, which could be caused by the substitutional diffusion, necessary for the formation of α ferrite instead of α′-bcc martensite. The global microstructural evolution, at the specimens 0_MA_1000 and 0_MA_1100, reflect the general decreasing tendency of the amount of α′-bcc martensite with increasing of pre-straining degree (Pricop et al., 2015b).

Aiming to overlap MA on the effects of heat treatment and pre-straining degree, fifteen sets of specimens, with three fractions of mechanically alloyed powders (0, 10, and 20 vol.%), were heat treated to the above five temperatures (700, 800, . . ., 1,100°C) before being pre-strained with various deformation degrees up to 4%. The formation of thermally induced α′-bcc martensite was revealed, as a particularity of these P/M-MA'ed alloys. Martensite plates became finer with the increase of MA'ed fraction, which enhanced a global increasing tendency of the amount of α′-bcc martensite on behalf of the amount of γ-fcc austenite (Mihalache et al., 2015). It has been concluded that internal friction, determined statically and dynamically, experienced an increasing trend with pre-straining degree, heat treatment temperature and MA'ed fraction (Mihalache et al., 2017).

A closer look was taken to the unusual decrease of α′-bcc martensite amount, with the increase of pre-straining degree at the specimens sintered from as-blended powders and heat treated to elevated temperatures. XRD patterns were recorded on specimens 0_MA_1000, in initial state and pre-strained with 2, 3, and 3.42%, as illustrated in **Figure 9** (Pricop et al., 2018).

In initial state, the amount of α′-bcc martensite is over 44%, much larger than that of ε-hcp martensite, 24%. With the increase of pre-straining degree to 2, 3, and 3.42%, the amount of α′-bcc martensite decreased to 23.9, 20.9, and 20.8% while that of ε-hcp martensite increased to 36, 38.8, and 38.9%, respectively. These data suggest ε-hcp martensite is stress-induced during pre-straining while thermally induced α′-bcc martensite is detwinned and reverts to γ-fcc austenite (Pricop et al., 2018). Similar results were obtained by Saito et al. and Amini et al. The former observed the formation of the γ-fcc and ε-hcp phases from the α-bcc phase due to diffusion of Mn and Si atoms into the Fe matrix (Saito et al., 2014) and the latter performed MA on Fe-32Mn-6Si and found that the $\alpha' \rightarrow \gamma$ phase transition occurred during the ball milling process (Amini et al., 2013).

The main shortcomings are related to the higher amount of α′-bcc martensite in the specimens sintered from MA'ed powders while those sintered from as-blended powders experienced opposing variation tendencies of thermally induced α′-bcc martensite: to increase, at specimens heat treated below 900°C and to decrease, at specimens heat treated above 1,000°C. Nevertheless, since MA contributed to porosity degree decrease, martensite plate refinement and internal friction increase, further studies must be focused on the effects of pre-straining degree and heat treatment temperature to the tendency of thermally

induced α′-bcc martensite to become detwinned and to revert to γ-fcc austenite.

## PARTICULARITIES OF α′-bcc MARTENSITE

The typical aspect of α′-bcc martensite is represented under the form of intersection areas between ε-hcp martensite plates. At P/M-MA'ed FeMnSiCrNi, heat treated at 1,100°C, this morphology is influenced by MA degree, as exemplified by **Figure 10** (Pricop et al., 2013).

Pre-strained specimens 0_MA_1100 and 50_MA_1100 were etched with a solution of 1.2% $K_2S_2O_5$ + 1% $NH_4HF_2$ in 100 ml distilled water and covered with Au film by an EDWARDS S150 deposition device. The SEM micrographs show a typical aspect of ε-hcp martensite and some dark regions, at the intersection of ε plates, which were associated with α′-bcc martensite. Obviously, the structure of 50_MA_1100 specimen, from **Figure 10b**, reveals a larger amount of α′-bcc martensite (Pricop et al., 2013).

An explanation for the decreasing tendency of the amount of α′-bcc martensite, with increasing pre-straining degree at specimens 0_MA_1100, was observed by investigating their sub-structure by HR-SEM, as shown in **Figure 11** (Pricop et al., 2018).

The grain boundary between α′-bcc and ε-hcp martensite regions, from **Figure 11a** is magnified in **Figure 11b**. Besides the typical spacing of 60 nm, between ε-hcp martensite plates, an internal sub-band is identified by an orange arrow in α′-bcc martensite. When analyzing the parallel array of α′-bcc martensite plates, from **Figure 11c**, the high resolution detail from **Figure 11d** reveals a spacing of 20 nm between internal sub-bands. We assumed that these sub-bands, in thermally induced α′-bcc martensite, hinder the nucleation and growth of α′ stress-induced martensite (Pricop et al., 2018).

A series of systematic measurements, performed by AFM, revealed a thinning tendency of martensite plate widths, from 1 to 2 μm at 0_MA specimens, to 0.78–0.97 μm at 20_MA specimens. This refining tendency, caused by the increase of MA'ed powder fraction is in good agreement with the structural analysis results observed by HR-SEM (Pricop et al., 2018). In addition, it was noticed that the chemical composition of the martensite plates is independent of the heat treatment temperature and thermally induced martensite plates preferably formed in Fe-rich, Mn-depleted regions (Cimpoesu et al., 2018).

The main shortcoming of present common scientific belief on α′-bcc martensite, in FeMnSi-based SMAs, is its detrimental effect of shape memory recovery. Further research need to be focused of the substructure of thermally induced α′-bcc martensite. The effects of its internal 20 nm-spaced sub-bands on the nucleation and growth of α′ stress-induced martensite require in-depth high resolution microscopy observations.

## DYNAMIC BEHAVIOR

The dynamic behavior of P/M-MA'ed FeMnSiCrNi specimens, hot rolled and heat treated, was investigated by DMA in temperature scan (TS) and strain sweep (SS) modes. Typical TS-DMA diagrams were presented in **Figure 6**, displaying the variations with temperature of storage modulus ($E'$) and internal friction (tanδ). The former experienced a local hardening ($\Delta E'$) and the latter displayed two maxima associated with: (i) antiferromagnetic-paramagnetic transition overlapped with the reversion to γ (fcc) austenite of α′-(bcc) martensite and (ii) the reversion of ε-hcp martensite reversion to γ-fcc austenite. SS-DMA tests were performed at three constant temperatures: $T_1$ = RT, (ii) $T_2 < A^{\varepsilon}_{50}$ and (iii) $T_3 > A^{\varepsilon}_{50}$ (the temperature of second tan δ maximum). The variations of $E'$ and tanδ with strain amplitude, in the case of specimen 0_MA_700, are summarized in **Figure 12** (Pricop et al., 2018).

The curves correspond to three SS cycles, *c1*, *2*, *3* as well as their average value, *avg*. At RT, in **Figure 12A** the storage modulus plateau noticed between 0.02 and 0.06 strain amplitudes can be associated with the stress-induced formation of ε-hcp martensite because, as long as martensite is stress induced, $E'$ value remained almost constant at about 128 GPa. In the other figures there are steeper increases of $E'$ and no plateaus are noticeable, since no martensite can be stress induced above $A^{\varepsilon}_{50}$. The specimen tested at $T_2 < A^{\varepsilon}_{50}$, contains a mixture of martensitic and austenitic phases, experienced the highest values of tanδ and $E'$ in **Figure 12B** (Pricop et al., 2018). The presence of this modulus plateau recommends P/M-MA'ed Fe-Mn-Si-Cr-Ni SMAs as potential candidates for RT-dampers, under the form of coupling rings of vibrating pipes (Popa et al., 2019).

The main shortcoming is the difficulty to increase internal friction at room temperature by creating bi-phasic structures (martensite/austenite). Since the single present solution for internal friction enhancement are stress-induced martensitic transformations, further studies are necessary in order to explain the in-depth relationship between stress-induced formation of martensite, storage modulus plateau and internal friction.

## SHAPE MEMORY EFFECT AND APPLICATIONS

Due to the lack of thermoelasticity, Fe-Mn-Si-based SMAs are unable to deliver work-generating SME. Yet, they are successful in developing free-recovery SME, with great potential for self-healing phenomena (Lutz et al., 2016) and constrained-recovery SME, applicable for couplings development.

The succession of bending-heating-cooling represents the most practical way to emphasize free-recovery SME. A lamellar specimen is bent, at RT, around a cylindrical caliber then heated at 600°C and SME is expressed as a function of the rotation angles (Söyler et al., 2014) or the successive positions of the free end of the specimen, monitored by video control. In order to get a better SME response, a training procedure can be applied by repetitively applying the bending-heating-cooling succession (Pricop et al., 2018).

The evolution of a lamellar 40_MA_1000 specimen, containing 46.8% α′-bcc and 25.5% ε-hcp martensite, is illustrated in **Figure 13**, during five training cycles (Mocanu et al., 2018).

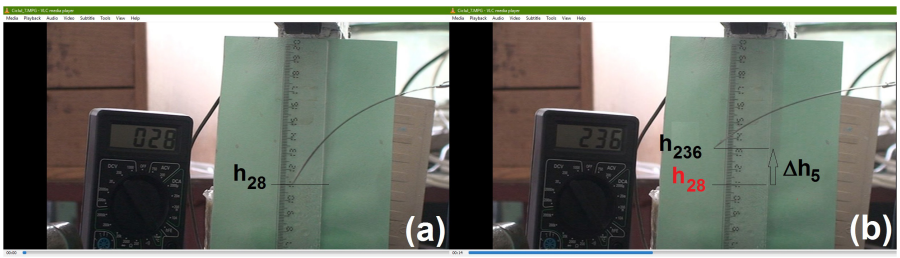


**FIGURE 13 |** Free-recovery SME training of a 40_MA_1000 lamellar specimen subjected to bending: **(a)** the start of 1st cycle; **(b)** the end of 5th cycle (reproduced after Mocanu et al., 2018, with permission granted by Springer Nature).

**TABLE 1 |** Evolution of training parameters.

| Cycle number | Temperature increase, $\Delta T$ (°C) | Maximum heating time, $\Delta t$ (s) | Maximum vertical displacement, $\Delta h$ (mm) | Average displacement rate | |
|---|---|---|---|---|---|
| | | | | in time, $\Delta h/\Delta t$ (mm/s) | with temperature, $\Delta h/\Delta T$ (mm/°C) |
| 1 | 228 | 9 | 15 | 1.07 | 0.066 |
| 2 | 270 | 21 | 16 | 0.76 | 0.059 |
| 3 | 135 | 36 | 19 | 0.53 | 0.141 |
| 4 | 219 | 17 | 20.5 | 1.21 | 0.094 |
| 5 | 208 | 14 | 24 | 1.71 | 0.115 |

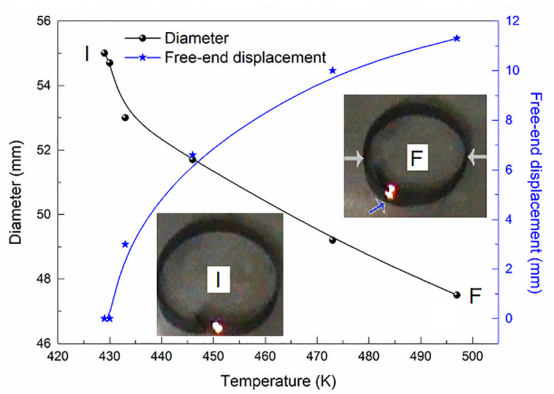


**FIGURE 14 |** Details of the training procedure applied to a 50_MA pipe-coupling ring subjected to free recovery SME, with opposite gray horizontal arrows indicating diameter shrinkage and blue tilted arrow emphasizing free-end displacement, from initial (I) to final (F) stages and variations of diameter and free-end displacement, during heating (modified after Bujoreanu, 2015).

**Figure 13a** shows the position of specimen's free end at 28°C, designated at $h_{28}$. During each cycle, a mobile gas lamp was used to heat up the specimen and a water spray to cool it down, both being moved along its entire length. Then the specimen was released and bent again against the caliber. The evolution of the training parameters: $\Delta T$-temperature increase, $\Delta t$-maximum heating time, $\Delta h$-maximum vertical displacement, and average displacement rates in time ($\Delta h/\Delta t$) and with temperature ($\Delta h/\Delta T$) are summarized in **Table 1**, for the five cycles. In **Figure 13b**, during heating up to 236°C, in the 5th cycle, the free end reached the position designated $h_{236}$, which gives a total displacement $\Delta h_5$ = 24 mm and an average displacement rate of 1.71 mm/s (Mocanu et al., 2018).

As mentioned above, P/M-MA'ed FeMnSiCrNi SMAs have the potential to be used for the development of coupling rings, meant to connect vibrating pipes that transport turbulent fluids, where dynamic stiffness is one of the key properties, because vibration could contribute to the accidental opening of coupling ring.

Pipe-coupling rings were produced by gradually heating lamellar specimens and rounding them, between outer and inner calibers. One example of the training procedure of a pipe coupling manufactured from a 50_MA lamellar specimen is shown in **Figure 14** (Bujoreanu, 2015).

**Figure 14** illustrates the initial and final training stages of the ring. The evolutions of rings diameter and free-end displacement with temperature, indicated by arrows, were monitored by cinematographic analysis and shown in the **Figure 14**.

The main shortcoming is related to the low value of shape recovery degree determined according to the beam bending model (Park et al., 2015). Further studies are necessary in order to increase the strokes developed by free-recovery SME and to develop fastening systems with advanced damping capacity, meant to safely connect oscillating part ends.

## CONCLUDING REMARKS AND FUTURE TRENDS

By summarizing the results reviewed in the above sections the following concluding remarks can be drawn, concerning P/M-MA'ed Fe-14Mn-6Si-9Cr-5Ni SMAs:

1. The use of over 8:1 BPR values and minimum 4 h of milling, in the presence of surfactant are found useful to obtain compositionally homogeneous composite particles having an average particle size of 10–20 μm which may easily be consolidated into bulk materials having enough relative density.
2. In thermally cycled powder mixtures, MA increased the thermal ranges of magnetic transition of Ni while the sintered powder compacts remained highly brittle, even after hot rolling and heat treatment, due to a porosity degree of 16.85%.
3. As an effect of increasing the fraction of MA'ed powders, porosity degree decreased to 2.51% at 50_MA, martensite plate variants became more diversified and more complexly intersected since more γ-fcc austenite transformed mostly to α′-bcc martensite during heat treatment, at temperatures as high as 1,200°C, both at short and long holding periods of time in low vacuum, argon or nitrogen.
4. At the specimens sintered from as-blended powders, the increase of pre-straining degree caused opposing variation tendencies of α′-bcc martensite: (i) to increase, at specimens 0_MA_700, 0_MA_800 and 0_MA_900 and (ii) to decrease, at specimens 0_MA_1000 and 0_MA_1100. At 0_MA_1000, ε-hcp martensite was stress-induced during pre-straining while thermally induced α′-bcc martensite was detwinned and reverted to γ-fcc austenite. Internal friction, determined statically and dynamically, experienced an increasing trend with pre-straining degree, heat treatment temperature and MA'ed fraction.
5. The substructure of thermally induced α′-bcc martensite contained internal sub-bands with 20 nm-spacing which hindered the nucleation and growth of α′ stress-induced martensite. Increasing the fraction of MA'ed powders, from 0 to 20%vol. caused a thinning tendency of martensite plate widths, from 1–2, to 0.78–0.97 μm.
6. DMA performed during heating emphasized a local increase of storage modulus ($\Delta E'_{max}$ = 19 GPa) and two internal friction maxima associated with: (i) antiferromagnetic-paramagnetic transition overlapped with the reversion to γ (fcc) austenite of α′-(bcc) martensite and (ii) the reversion of ε-hcp martensite reversion to γ-fcc austenite. DMA performed isothermally at RT highlighted a storage modulus plateau, between 0.02 and 0.06 strain amplitude, associated with the stress-induced formation of ε-hcp martensite because.
7. After five thermomechanical training cycles, a 40_MA_1000 lamellar specimen, containing 46.8% α′-bcc and 25.5% ε-hcp martensites, developed a total displacement $\Delta h_5$ = 24 mm and an average displacement rate of 1.71 mm/s.
8. Coupling rings with advanced damping capacity, meant to connect vibrating pipes that transport turbulent fluids, were produced and trained from lamellar specimens.
9. Further research efforts are necessary in order to develop the advanced processing, characterization and implementation of P/M-MA'ed Fe-14Mn-6Si-9Cr-5Ni SMAs which have the potential to contribute to the production of simple high damping fastening systems.

## AUTHOR CONTRIBUTIONS

BP organized the figures and requested the utilization permissions from corresponding publishing houses. BÖ and AS organized the section concerning P/M-MA processing. LB arranged the manuscript and managed the correspondence. All authors contributed to the article and approved the submitted version.

## REFERENCES


Amini, R., Shamsipoor, A., Ghaffari, M., Alizadeh, M., and Okyay, A. K. (2013). Phase transformation during mechano-synthesis of nanocrystalline/amorphous Fe-32Mn-6Si alloys. *Mater. Char.* 84, 169–174. doi: 10.1016/j.matchar.2013.07.017

Arruda, G. J., Buono, V. T. L., and Andrade, M. S. (1999). The influence of deformation on the microstructure and transformation temperatures of Fe–Mn–Si–Cr–Ni shape memory alloys. *Mater. Sci. Eng. A* 273–275, 528–532. doi: 10.1016/s0921-5093(99)00393-7

Aydogmus, T., and Bor, A. S. (2011). Production and characterization of porous TiNi shape memory alloys. *Turkish J. Eng. Env. Sci.* 35, 69–82. doi: 10.3906/muh-1007-1127

Bahador, A., Hamzah, E., Kondoh, K., Kawahito, Y., Junko, U., and Abu Bakar, T. A. (2017). Mechanical and superelastic properties of disk-laser welded Ti-Ni shape-memory alloys produced by powder metallurgy. *J. Mater. Proc. Tech.* 248, 198–206. doi: 10.1016/j.jmatprotec.2017.05.019

Bahador, A., Junko, U., Mizutani, M., Hamzah, E., Yusof, F., and Kondoh, K. (2020). High-brightness and high-power laser welding of powder metallurgy shape memory alloy: welding-parameter-dependent microstructure. *J. Mater. Eng. Perform.* 29:987. doi: 10.1007/s11665-020-04597-0

Berns, H., and Theisen, W. (2008). *Ferrous Materials: Steel and Cast Iron*. Berlin: Springer, 190–207.

Bracke, L., Mertens, G., Penning, J., De Cooman, B. C., Liebeherr, M., and Akdut, N. (2006). Influence of phase transformations on the mechanical properties of high-strength austenitic Fe-Mn-Cr steel. *Metall. Mater. Trans. A* 37A, 307–317. doi: 10.1007/s11661-006-0002-5

Bujoreanu, L. G. (2015). Development of shape memory and superelastic applications of some experimental alloys. *J Optoelectron. Adv. M.* 17, 1437–1443.

Bujoreanu, L. G., Stanciu, S., Ozkal, B., Comaneci, R. I., and Meyer, M. (2009). "Comparative study of the structures of Fe-Mn-Si-Cr-Ni shape memory alloys obtained by classical and by powder metallurgy, respective1y," in *ESOMAT 2009 - European Symposium on Martensitic Transformations*, eds P. Šittner, L. Heller, and V. Paidar (Paris: EDP Sciences), 05003. doi: 10.1051/esomat/200905003

Bulbuc, V., Pricop, B., Popa, M., Mihalache, E., Özkal, B., and Bujoreanu, L. G. (2019). Thermomechanical processing effects on the structure and properties of Fe-based SMAs. I. Evolution of phase structure. *IOP Conf. Series* 485:012004. doi: 10.1088/1757-899x/485/1/012004

Cimpoesu, N., Mihalache, E., Lohan, N. M., Suru, M. G., Comăneci, R. I., Özkal, B., et al. (2018). Structural-morphological fluctuations induced by thermomechanical treatment in a Fe – Mn – Si shape memory alloy. *Met. Sci. Heat Treat.* 60, 471–477. doi: 10.1007/s11041-018-0303-5

Dang, S., Li, Y., Zou, Q., Wang, M., Xiong, J., and Luo, W. (2019). Progress in Fe-Mn-Si based shape memory alloys prepared by mechanica1 alloying and powder metallurgy. *J. Mater. Eng.* 47, 18–25.

Dogan, A., and Arslan, H. (2012). Effect of ball-milling conditions on microstructure during production of Fe-20Mn-6Si-9Cr shape memory alloy powders by mechanical alloying. *J. Therm. Anal. Ca1orim.* 109, 933–938. doi: 10.1007/s10973-011-1809-x

Druker, A., Perotti, A., Esquivel, I., and Malarría, J. (2014). A manufacturing process for shaft and pipe couplings of Fe–Mn–Si–Ni–Cr shape memory alloys. *J. Mater. Design* 56:878. doi: 10.1016/j.matdes.2013.11.032

Dunne, D. (2012). "Shape memory in ferrous alloys," in *Diffusionless Transformations, High Strength Steels, Modelling and Advanced Analytical Techniques. Phase Transformations in Steels*, Vol. 2, eds E. Pereloma and D. V. Edmonds (Cambridge: Woodhead), 83–125. doi: 10.1533/9780857096111.1.83

He, Q., Jia, C., and Meng, J. (2006). Inf1uence of iron powder particle size on the microstructure and properties of Fe3Al intermetallics prepared by mechanical alloying and spark plasma sintering. *Mater. Sci. Eng. A.* 428, 314–318. doi: 10.1016/j.msea.2006.05.024

Kajiwara, S. (1999). Characteristic features of shape memory effect and related transformation behavior in Fe-based alloys. *Mat. Sci. Eng. A* 273–275, 67–88. doi: 10.1016/s0921-5093(99)00290-7

Li, J. C., Zhao, M., and Jiang, Q. (2000). Alloy design of Fe-Mn-Si-Cr-Ni shape-memory alloys related to stacking-fault energy. *Metall. Mater. Trans. A* 31, 581–584.

Liu, T., Liu, H. Y., Zhao, Z. T., Ma, R. Z., Hu, T. D., and Xie, Y. N. (1999). Mechanical alloying of Fe- Mn and Fe-Mn-Si. *Mater. Sci. Eng. A.* 271, 8–13. doi: 10.1016/s0921-5093(98)01022-3

Lutz, A., Van den Berg, O., Wielant, J., De Graeve, I., and Terryn, H. (2016). A multiple-action self-healing coating. *Front. Mater.* 2:73.

Ma, J., and Karaman, I. (2010). Expanding the repertoire of shape memory alloys. *Science* 327, 1468–1469. doi: 10.1126/science.1186766

Maruyama, T., Kurita, T., Kozaki, S., Andou, K., Farjami, S., and Kubo, H. (2008). Innovation in producing crane rail fishplate using Fe–Mn–Si–Cr based shape memory alloy. *J. Mater. Sci. Technol.* 24, 908–912. doi: 10.1179/174328408x302585

Mazzer, E. M., Gargarella, P., Cava, R. D., Bolfarini, C., Galano, M., and Kiminami, C. S. (2017). Effect of dislocations and residual stresses on the martensitic transformation of Cu-Al-Ni-Mn shape memory alloy powders. *J. Alloy Compd.* 723, 841–849. doi: 10.1016/j.jallcom.2017.06.312

Mihalache, E., Pricop, B., Comăneci, R. I., Suru, M. G., Lohan, N. M., Mocanu, M., et al. (2017). Structural Effects of Thermomechanical Processing on the Static and Dynamic Responses of Powder Metallurgy Fe-Mn-Si Based Shape Memory Alloys. *Adv. Sci. Technol.* 97, 153–158. doi: 10.4028/www.scientific.net/ast.97.153

Mihalache, E., Pricop, B., Suru, M. G., Lohan, N. M., Comăneci, R. I., Istrate, B., et al. (2015). Factors influencing martensite transitions in Fe-based shape memory alloys, Matec Web of Conferences. *Paris EDP Sci.* 33:04002. doi: 10.1051/matecconf/20153304002

Mocanu, M., Mihalache, E., Pricop, B., Borza, F., Grigoraş, M., Comăneci, R. I., et al. (2018). "The Influence of α′(bcc) Martensite on the Dynamic and Magnetic Response of Powder Metallurgy Fe-Mn-Si-Cr-Ni Shape Memory Alloys," in *Proceedings of the International Conference on Martensitic Transformations*, eds A. P. Stebner and G. B. Olson (Chicago: Springer), 99–108. doi: 10.1007/978-3-319-76968-4_16

Moriya, Y., Kimura, H., Ishizaki, S., Hashizume, S., Suzuki, S., Suzuki, H., et al. (1991). Properties of Fe-Cr-Ni-Mn-Si (-Co) shape memory alloys. *J. Phys. IV C* 4, 433–437.

Murakami, M., Otsuka, H. H., and Matsuda, S. (1987a). Improvement in shape memory effect for Fe-Mn-Si alloys. *Trans. ISIJ* 27:B89.

Murakami, M., Otsuka, H., Suzuki, H., and Matsuda, S. (1987b). Effect of alloying content, phase and magnetic transformation on shape memory effect of Fe-Mn-Si alloys. *Trans. ISIJ* 27:B88.

Murakami, M., Suzuki, H., and Nakamura, Y. (1987c). Effect of silicon on the shape memory effect of polycrystalline Fe-Mn-Si alloys. *Trans. ISIJ* 27:B87.

Oro, R., Hryha, E., Campos, M., and Torralba, J. M. (2014). Effect of processing conditions on microstructural features in Mn-Si sintered steels. *Mat. Char.* 95, 105–117. doi: 10.1016/j.matchar.2014.06.011

Otsuka, H. (1991). Fe-Mn-Si Based Shape Memory Alloys. *MRS Proc.* 246:309. doi: 10.1557/PROC-246-309

Otsuka, H., Yamada, H., Maruyama, T., Tanahashi, H., Matsuda, S., and Murakami, M. (1990). Effects of alloying additions on Fe-Mn-Si shape memory alloys. *Trans. ISIJ* 30, 674–679. doi: 10.2355/isijinternational.30.674

Paleu, V., Gurău, G., Comăneci, R. I., Sampath, V., Gurău, C., and Bujoreanu, L. G. (2018). A new application of Fe-28Mn-6Si-5Cr (mass%) shape memory alloy, for self adjustable axial preloading of ball bearings. *Smart Mater. Struct.* 27:075026. doi: 10.1088/1361-665X/aac4c5

Park, J., Headings, L. M., Dapino, M. J., Baur, J. W., and Tandon, G. P. (2015). Investigation of interfacial shear stresses, shape fixity, and actuation strain in composites incorporating shape memory polymers and shape memory alloys. *Front. Mater.* 2:12. doi: 10.3389/fmats.2015.00012

Peng, H., Chen, J., Wang, Y., and Wen, Y. (2017). Key factors achieving large recovery strains in po1ycrystalline Fe-Mn-Si based shape memory alloys: a review. *Adv. Eng. Mater.* 20, 1–18.

Peng, H., Wang, G., Wang, S., Chen, J., Mac Laren, I., and Wen, Y. (2018). Key criterion for achieving giant recovery strains in polycrystalline Fe-Mn-Si based shape memory alloys. *Mater. Sci. Eng. A.* 712, 37–49. doi: 10.1016/j.msea.2017.11.071

Popa, M., Pricop, B., Bulbuc, V., Mihalache, E., Özkal, B., and Bujoreanu, L. G. (2019). Thermomechanical processing effects on the structure and properties of Fe-based SMAs. II. Evolution of damping behavior. *IOP Conf. Series* 485:012023. doi: 10.1088/1757-899x/485/1/012023

Pricop, B., Mihalache, E., Lohan, N. M., Istrate, B., Mocanu, M., Özkal, B., et al. (2015a). Powder metallurgy and mechanical alloying effects on the formation of thermally induced martensite in an FeMnSiCrNi SMA. *Matec Web Conf. Paris EDP Sci.* 33:04004. doi: 10.1051/matecconf/20153304004

Pricop, B., Söyler, U., Özkal, B., Suru, M. G., Lohan, N. M., Comaneci, R. I., et al. (2015b). A study of martensite formation in powder metallurgy Fe-Mn-Si-Cr-Ni shape memory alloys. *Mater. Today Proc.* 2, 789–792.

Pricop, B., Mihalache, E., Stoian, G., Borza, F., Özkal, B., and Bujoreanu, L. G. (2018). Thermo-mechanical effects caused by martensite formation in powder metallurgy FeMnSiCrNi shape memory alloys. *Powder Met.* 61, 348–356. doi: 10.1080/00325899.2018.1492773

Pricop, B., Özkal, B., Söyler, U., Van Humbeeck, J., Lohan, N. M., Suru, M. G., et al. (2014). Influence of mechanically alloyed fraction and hot rolling temperature in the last pass on the structure of Fe-14Mn-6Si-9Cr-5Ni (mass.%) shape memory alloys processed by powder metallurgy. *Optoelectron. Adv. Mat.* 8, 247–250.

Pricop, B., Özkal, B., Söyler, U., Van Humbeeck, J., Lohan, N. M., Suru, M. G., et al. (2016). Structural changes caused by high-temperature holding of powder shape memory alloy Fe-14Mn-6Si-Cr-5Ni. *Met. Sci. Heat Treat.* 57, 553–558. doi: 10.1007/s11041-016-9921-y

Pricop, B., Söyler, U., Comaneci, R. I., Özkal, B., and Bujoreanu, L. G. (2010). Mechanica1 cycling effects at Fe-Mn-Si-Cr-Ni SMAs obtained by powder metallurgy. *Phys. Proc.* 10, 125–131.

Pricop, B., Söyler, U., Lohan, N. M., Özkal, B., Bujoreanu, L. G., Chicet, D., et al. (2012). Therma1 behavior of mechanically alloyed powders used for producing an Fe- Mn-Si-Cr-Ni shape memory alloy. *J. Mater. Eng. Perform.* 21, 2407–2416.

Pricop, B., Söyler, U., Lohan, N. M., Özkal, B., Chicet, D., David, A., et al. (2011). Mechanica1 alloying effects on the thermal behavior of a Fe-Mn-Si-Cr-Ni shape memory alloy under powder form. *Optoelectron. Adv. Mat.* 5, 555–561.

Pricop, B., Söyler, U., Özkal, B., Lohan, N. M., Paraschiv, A. L., Suru, M. G., et al. (2013). Inf1uence of Mechanical Alloying on the Behavior of Fe-Mn-Si-Cr-Ni Shape Memory Alloys Made by Powder Metallurgy. *Materials Science Forum.* 739, 237–241.

Saito, T., Kapusta, C., and Takasaki, A. (2014). Synthesis and characterization of Fe-Mn-Si shape memory alloy by mechanical alloying and subsequent sintering. *Mater. Sci. Eng. A.* 592, 88–94.

Sato, A., Chishima, E., Soma, K., and Mori, T. (1982). Shape memory effect in γ ↔ ε transformation in Fe-30Mn-1Si alloy single crystals. *Acta Metall.* 30, 1177–1183.

Sawaguchi, T., Bujoreanu, L. G., Kikuchi, T., Ogawa, K., and Yin, F. (2008). Effects of Nb and C in Solution and in NbC form on the transformation-related internal friction of Fe–17Mn (mass%) alloys. *ISIJ* 48, 99–106.

Sawaguchi, T., Kikuchi, T., Ogawa, K., Kajiwara, S., Ikeo, Y., Kojima, M., et al. (2006). Development of prestressed concrete using Fe-Mn-Si-based shape memory alloys containing NbC. *Mater. Trans.* 47, 580–583.

Shahverdi, M., Czaderski, C., and Motavalli, M. (2016). Iron-based shape memory alloys for prestressed near surface mounted strengthening of reinforced concrete beams. *Constr. Build. Mater.* 112, 28–38.

Söyler, A. U., Özkal, B., and Bujoreanu, L. G. (2010). Sintering Densification and Microstructural Characterization of Mechanical Alloyed Fe-Mn-Si based Powder Metal System, TMS 2010. *Suppl. Proc.* 3, 785–792.

Söyler, A. U., Özkal, B., and Bujoreanu, L. G. (2011). Investigation of Mechanical Alloying Process Parameters on Fe-Mn-Si Based System, TMS 2011. *Suppl. Proc.* 1, 577–583.

Söyler, A. U., Özkal, B., and Bujoreanu, L. G. (2014). Improved shape memory characteristics of Fe-14Mn-6Si-9Cr-5Ni alloy via mechanical alloying. *J. Mater. Eng. Perf.* 23, 2357–2361.

Spiridon, I. P., Pricop, B., Suru, M. G., Paraschiv, A. L., Lohan, N. M., and Bujoreanu, L. G. (2013). The influence of heat treatment atmosphere and maintaining period on the homogeneity degree of a Fe-Mn-Si-Cr-Ni shape memory alloy obtained through powder metallurgy. *J. Optoelectron. Adv. M.* 15, 730–733.

Stanford, N., Dunne, D., and Li, H. (2008). Re-examination of the effect of NbC precipitation on shape memory in Fe–Mn–Si-based alloys. *Scripta Mater.* 58, 583–586.

Sun, L., Huang, W. M., Ding, Z., Zhao, Y., Wang, C. C., Purnawali, H., et al. (2012). Stimulus-responsive shape memory materials: A review. *Mater Design.* 33, 577–640.

Wen, Y.H., Peng, H. B., Raabe, D., Gutierrez-Urrutia, I., Chen, J., and Du, Y. Y. (2014). Large recovery strain in Fe-Mn-Si-based shape memory steels obtained by engineering annealing twin boundaries. *Nature Comm.* 5:4964. doi: 10.1038/ncomms5964

Xu, Z., Hodgson, M. A., and Cao, P. (2015). A comparative study of powder metallurgical (PM) and wrought Fe-Mn-Si alloys. *Mater. Sci. Eng. A.* 630, 116–124.

Xu, Z., Hodgson, M. A., and Cao, P. (2016). Effects of mechanical milling and sintering temperature on the densification, microstructure and tensile properties of the Fe-Mn-Si powder compacts. *J. Mater. Sci. Technol.* 32, 1161–1170.

Zhang, Z., Sandstroma, R., Frisk, K., and Salwen, A. (2003). Characterization of intermetallic Fe-Mn-Si powders produced by casting and mechanical ball milling. *Powder Tech.* 137, 139–147.

**Conflict of Interest:** AS has been employed by company TETA Glass Technologies.

The remaining authors declare that the research was conducted, between 2009 and 2019, in the absence of any commercial or financial relationships that could be construed as a potential conflict of interest.